



Multiple Stellar Populations in Metal-poor Globular Clusters with JWST: A NIRCам View of M92

Tuila Ziliotto¹, Antonino Milone^{1,2}, Anna F. Marino^{2,3}, Aaron L. Dotter⁴, Alvio Renzini², Enrico Vesperini⁵, Amanda Karakas^{6,7}, Giacomo Cordoni^{1,2}, Emanuele Dondoglio¹, Maria V. Legnardi¹, Edoardo P. Lagioia¹, Anjana Mohandasan¹, and Sarah Baimukhametova¹

¹ Dipartimento di Fisica e Astronomia Galileo Galilei, Univ. di Padova, Vicolo dell'Osservatorio 3, Padova, I-35122, Italy; tuila.ziliotto@unipd.it

² Istituto Nazionale di Astrofisica—Osservatorio Astronomico di Padova, Vicolo dell'Osservatorio 5, Padova, I-35122, Italy

³ Istituto Nazionale di Astrofisica—Osservatorio Astrofisico di Arcetri, Largo Enrico Fermi, 5, Firenze, I-50125, Italy

⁴ Department of Physics and Astronomy, Dartmouth College, 6127 Wilder Laboratory, Hanover, NH 03755, USA

⁵ Department of Astronomy, Indiana University, Bloomington, IN 47401, USA

⁶ School of Physics and Astronomy, Monash University, VIC 3800, Australia

⁷ Centre of Excellence for Astrophysics in Three Dimensions (ASTRO-3D), Melbourne, VIC, Australia

Received 2023 April 6; revised 2023 May 26; accepted 2023 June 13; published 2023 August 2

Abstract

Recent work on metal-intermediate globular clusters (GCs) with $[\text{Fe}/\text{H}] = -1.5$ and -0.75 has illustrated the theoretical behavior of multiple populations in photometric diagrams obtained with the JWST. These results are confirmed by observations of multiple populations among the M dwarfs of 47 Tucanae. Here we explore multiple populations in metal-poor GCs with $[\text{Fe}/\text{H}] = -2.3$. We take advantage of synthetic spectra and isochrones that account for the chemical composition of multiple populations to identify photometric diagrams that separate the distinct stellar populations of GCs. We derive high-precision photometry and proper motion for main-sequence (MS) stars in the metal-poor GC M92 from JWST and Hubble Space Telescope images. We identify a first-generation (1G) and two main groups of second-generation ($2G_A$ and $2G_B$) stars and investigate their kinematics and chemical composition. We find isotropic motions with no differences among the distinct populations. The comparison between the observed colors of the M92 stars and the colors derived by synthetic spectra reveals that the helium abundances of $2G_A$ and $2G_B$ stars are higher than those of the 1G by $\Delta Y \sim 0.01$ and 0.04 , respectively. The m_{F090W} versus $m_{F090W} - m_{F277W}$ color–magnitude diagram shows that below the knee MS stars exhibit a wide color broadening due to multiple populations. We constrain the amount of oxygen variation needed to reproduce the observed MS width, which is consistent with results on red giant branch stars. We conclude that multiple populations with masses of ~ 0.1 – $0.8 M_\odot$ share similar chemical compositions.

Unified Astronomy Thesaurus concepts: Globular star clusters (656); Population II stars (1284); Stellar abundances (1577); Photometry (1234)

1. Introduction

In the past few decades, the Hubble Space Telescope (HST) has been instrumental in demonstrating that the color–magnitude diagrams (CMDs) of most globular clusters (GCs) consist of multiple sequences of stars. Each stellar sequence corresponds to a distinct stellar population with a characteristic chemical composition. The GCs typically host distinct groups of stars, one with the same chemical composition as halo field stars (first generation, 1G) and a second generation of stars (2G), which are typically enhanced in He, N, Na, and Al and depleted in C and O (see Bastian & Lardo 2018; Gratton et al. 2019; Marino et al. 2019; Milone & Marino 2022, for recent reviews).

The origin of multiple populations is one of the most debated topics of modern stellar astrophysics. Most scenarios of the formation of multiple populations suggest that GCs experienced multiple star formation episodes where 2G stars formed from material polluted by more massive 1G stars. The nature of the polluters is controversial. The main candidates include intermediate-mass asymptotic giant branch (AGB) and super-

AGB stars (Cottrell & Da Costa 1981; Dantona et al. 1983; D’Antona et al. 2016; Calura et al. 2019), fast-rotating massive stars (Decressin et al. 2007), massive interactive binaries (Renzini et al. 2022), and supermassive stars (Denissenkov & Hartwick 2014). Alternatively, the chemical enrichment of 2G stars could originate from processed gas ejected by massive binary systems or supermassive stars and accreted by pre-main-sequence stars in the proto-GCs (Bastian et al. 2013; Gieles et al. 2018).

Most photometric studies of multiple stellar populations are based on ultraviolet photometry from either HST (e.g., Milone et al. 2012b, 2017; Piotto et al. 2015; Lagioia et al. 2021; Milone & Marino 2022, and references therein) or ground-based facilities (e.g., Marino et al. 2008; Yong et al. 2008; Monelli et al. 2013; Jang et al. 2022; Lee 2022). Indeed, UV filters enclose spectral regions that are affected by molecules that include C, N, and O. Specifically, the HST filter F336W encompasses NH molecular bands, while the F275W filter includes the OH bands. The F410M and F438W filters include CH molecular bands, whereas the narrowband F280N filter encloses Mg lines. A similar conclusion can be extended to the Johnson–Cousins and Strömgren filters (Marino et al. 2008; Sbordone et al. 2011; Milone et al. 2020; VandenBerg 2022). The main limitation of studies based on UV photometry is that they are limited to stars of the upper main sequence (MS) or

brighter. Indeed, it is challenging to obtain high-precision UV photometry of faint stars with present-day facilities. On the contrary, HST photometry in the appropriate near-IR (NIR) bands, such as the F110W and F160W filters of the IR channel of the Wide Field Camera 3 (WFC3), is an efficient tool to identify stellar populations among M dwarfs (Milone et al. 2012b, 2019; Dondoglio et al. 2022).

Recently, Milone et al. (2023b) computed isochrones of different stellar populations in the James Webb Space Telescope (JWST)/NIRCam filters for metal-rich ($[\text{Fe}/\text{H}] = -0.75$) and metal-intermediate ($[\text{Fe}/\text{H}] = -1.5$) GCs. The results allowed them to identify photometric diagrams suitable for identifying and characterizing multiple stellar populations. In particular, NIRCam images are formidable tools to disentangle multiple populations among M dwarfs in the CMD region that ranges from the MS knee toward the H-burning limit. NIRCam observations confirm these theoretical results. Milone et al. (2023b) showed that the M dwarfs of 47 Tucanae span a wide F115W–F322W2 color interval. The color broadening is due to the different amounts of blanketing from molecules composed of oxygen (mostly water vapor) in the F322W2 filter, as 2G stars have lower oxygen and hence low H_2O content, compared to 1G stars that are oxygen-rich and hence H_2O -rich. Based on a pseudo-two-color diagram or “chromosome map” (ChM), Milone et al. (2023b) unveiled an extended first population and three main groups of second-population stars among the M dwarfs of 47 Tucanae with different oxygen abundances. Isochrones indicate that the diagrams composed of NIRCam photometry alone have poor sensitivity to multiple populations among stars that are brighter than the MS knee, with the exception of stars close to the tip of the red giant branch (RGB), where we expect that 1G and 2G stars exhibit different fluxes in certain NIRCam filters, like F277W and F460M. The magnitude difference is primarily due to the effect of H_2O and CO molecules in the atmospheres of these stars. The 2G stars, which are O-depleted with respect to the 1G, exhibit weaker lines of these molecules and hence brighter fluxes when compared to 1G stars (Salaris et al. 2019; Milone et al. 2023b).

In this work, we explore multiple populations with HST and JWST at low metallicities ($[\text{Fe}/\text{H}] = -2.3$). We first investigate the metal-poor GC M92 (NGC 6341; $[\text{Fe}/\text{H}] = -2.31$; 2010 version of the Harris 1996 catalog) and its multiple stellar populations by using images collected with HST and JWST. We compute isochrones that account for the chemical composition of 1G and 2G stars in metal-poor GCs to construct the photometric diagrams based on HST and NIRCam photometry that allow us to identify and characterize multiple populations at low metallicities. The paper is structured as follows. Section 2 describes the data set and the methods to derive high-precision photometry, astrometry, and proper motions. Section 3 is dedicated to the photometry of multiple stellar populations along the RGB and MS. The synthetic spectra and isochrones of 1G and 2G stars in metal-poor GCs are presented in Section 4, where we also infer the chemical composition of the multiple populations of M92. Section 5 provides the summary of the results and discussion.

2. Data and Data Reduction

To investigate multiple stellar populations in M92, we used both NIRCam data and images collected with the wide-field

channel of the Advanced Camera for Surveys (WFC/ACS) and the ultraviolet and visual channel of the WFC3 (UVIS/WFC3) on board HST. The main properties of the data set are summarized in Table 1.

We derived the photometry and astrometry of stars in all HST images with the computer program `img2xym`, originally developed by Anderson & King (2006) to reduce WFC/ACS images. In a nutshell, we separately measured the stellar fluxes and positions in each image using a spatially variable point-spread function (PSF) model plus a “perturbation PSF” that fine-tunes the fitting to account for small variations of the HST focus. The latter is derived using unsaturated, bright, and isolated stars, while the magnitudes of saturated stars are calculated as in Gilliland (2004). The various measurements of the magnitudes and positions are then averaged together to get the best estimates. We used a similar method to calculate the magnitudes and positions of stars in the NIRCam images. The difference is that we derived a spatially variable PSF model for each image based on the available unsaturated, bright, and isolated stars. To do this, we used the computer program `img2psf`, originally developed by Anderson et al. (2006) for images collected with the Wide Field Imager of the 2.2 m telescope in La Silla and adapted by Milone et al. (2023b) for NIRCam (see Milone et al. 2023b for details).

We corrected the stellar positions for the effects of the geometric distortions of the WFC/ACS, UVIS/WFC3, and short-wavelength modules of the NIRCam detectors by adopting the solutions by Anderson & King (2006), Bellini & Bedin (2009), Bellini et al. (2011), and Milone et al. (2023b), respectively. We calibrated the photometry into the Vega-mag system as in Milone et al. (2023a) and using the zero-points provided by the Space Telescope Science Institute webpage.⁸ Since we are interested in stars with high-precision photometry, we followed the recipe by Milone et al. (2023a) to select the relatively isolated stars that are well fit by the PSF model and have small photometric and astrometric uncertainties.

2.1. Proper Motions

We used multiepoch HST and JWST images and Gaia DR3 data (Gaia Collaboration et al. 2021) to derive the proper motions of the stars in the field of view of M92 and investigate the internal kinematics of the multiple stellar populations. The proper motions are derived by following the recipe by Milone et al. (2023a; see their Section 5.1). We separately reduced each group of images collected at the same epoch through the same filter and camera by using the methods described in Section 2 (see Table 1 for details on the data set). To avoid systematic errors in proper motions, we excluded from the analysis the images collected through the F225W, F275W, and F336W filters of UVIS/WFC3 (Bellini et al. 2011). We derived the astrometric and photometric catalog of each group of images and selected the reference frame of the F814W images from GO 10775 as a master frame. Six-parameter linear equations are used to transform the coordinates of the stars in each catalog into the master frame (Anderson & King 2006). To derive the proper motion of each star, we plotted the stellar displacements, expressed in milliarcseconds, relative to the

⁸ <https://www.stsci.edu/hst/instrumentation/acs/data-analysis/zero-points;>
<https://www.stsci.edu/hst/instrumentation/wfc3/data-analysis/photometric-calibration;>
<https://jwst-docs.stsci.edu/jwst-near-infrared-camera/nircam-performance/nircam-absolute-flux-calibration-and-zero-points>

Table 1
Description of the Images Used in This Paper

Mission	Camera	Filter	Date	$N \times \text{Exp. Time}$	Program	PI
HST	WFC/ACS	F814W	2002 Aug 27	0.5 s + 6 s + 100 s	9453	T. M. Brown
HST	WFC/ACS	F625W	2004 Aug 7	10 s + 3 × 120 s	10120	S. Anderson
HST	WFC/ACS	F658N	2004 Aug 7	2 × 350 s + 2 × 555 s	10120	S. Anderson
HST	WFC/ACS	F606W	2006 Nov 14	7 s + 4 × 140 s	10775	A. Sarajedini
HST	WFC/ACS	F814W	2006 Nov 14	7 s + 4 × 150 s	10775	A. Sarajedini
HST	UVIS/WFC3	F390W	2009 Oct 10	2 × 2 s + 2 × 348 s + 2 × 795 s	11664	T. M. Brown
HST	UVIS/WFC3	F555W	2009 Oct 10	1 s + 30 s + 2 × 665 s	11664	T. M. Brown
HST	UVIS/WFC3	F336W	2009 Oct 11	30 s + 2 × 425 s	11729	J. Holtzman
HST	UVIS/WFC3	F390M	2009 Oct 11	50 s + 2 × 700 s	11729	J. Holtzman
HST	UVIS/WFC3	F390W	2009 Oct 11	10 s	11729	J. Holtzman
HST	UVIS/WFC3	F395N	2009 Oct 10–11	90 s + 2 × 965 s	11729	J. Holtzman
HST	UVIS/WFC3	F410M	2009 Oct 11	40 s + 2 × 765 s	11729	J. Holtzman
HST	UVIS/WFC3	F467M	2009 Oct 11	40 s + 2 × 350 s	11729	J. Holtzman
HST	UVIS/WFC3	F547M	2009 Oct 11	5 s + 40 s + 400 s	11729	J. Holtzman
HST	WFC/ACS	F475W	2012 Aug 21	4 × 400 s	12116	J. Holtzman
HST	UVIS/WFC3	F275W	2013 Oct 22	2 × 707 s	13297	G. Piotto
HST	UVIS/WFC3	F336W	2013 Oct 22	2 × 304 s	13297	G. Piotto
HST	UVIS/WFC3	F438W	2013 Oct 22	59 s	13297	G. Piotto
HST	UVIS/WFC3	F275W	2014 Aug 3	2 × 819 s	13297	G. Piotto
HST	UVIS/WFC3	F336W	2014 Aug 3	2 × 304 s	13297	G. Piotto
HST	UVIS/WFC3	F438W	2014 Aug 3	57 s	13297	G. Piotto
HST	UVIS/WFC3	F225W	2019 Jun 28	3 × 30 s + 2 × 800 s + 3 × 805 s + 815 s + 820 s + 4 × 835 s	15173	J. S. Kalirai
HST	WFC/ACS	F814W	2021 Jan 24	35 s + 4 × 337 s	16289	M. Libralato
JWST	NIRCam	F090W	2022 Jun 20–21	4 × 311 s	1334	D. R. Weisz
JWST	NIRCam	F150W	2022 Jun 20–21	4 × 311 s	1334	D. R. Weisz
JWST	NIRCam	F277W	2022 Jun 20–21	4 × 311 s	1334	D. R. Weisz
JWST	NIRCam	F444W	2022 Jun 20–21	4 × 311 s	1334	D. R. Weisz

master frame against the time in years. We fitted these points with a weighted least-squares straight line and considered the slope as the best estimate of the proper motions (see Piotto et al. 2012; Milone et al. 2023a for details).

To derive the transformations, we used only the bright and unsaturated stars that are well fit by the PSF model according to the criteria of Section 2. Specifically, we calculated proper motions relative to a sample of cluster stars that are selected by using a two-step procedure. We initially selected stars that, based on their position on the CMDs, are cluster members and derived raw proper motions. Then, we improved the determination of the proper motions by deriving the transformations from those stars that, according to their kinematics, are not cluster members. As a consequence of this procedure, the cluster stars have null relative proper motions.

To transform the proper motions from the relative to the absolute scale, we identified the stars for which relative proper motions from HST and JWST and absolute proper motions from Gaia DR3 are available. We only considered stars with accurate Gaia DR3 proper motions according to the criteria by Cordoni et al. (2020b), which are based on the proper-motion uncertainties and the values of the renormalized unit weight error, the `astrometric_gof_al` (`As_gof_al`) parameter.

3. Multiple Stellar Populations in M92

In the context of multiple populations, M92 is a well-studied cluster. The ChM of RGB stars reveals an extended 1G sequence, which hosts $30.4\% \pm 1.5\%$ of the cluster stars, and two distinct groups of 2G stars (Milone et al. 2017, 2018b). Recent works based on multiband HST photometry indicate that the extended 1G is due to internal

metallicity variations of $[\text{Fe}/\text{H}] \sim 0.15$ dex (Legnardi et al. 2022), and 2G stars with extreme chemical compositions are enhanced in helium mass fraction by 0.039 ± 0.006 with respect to the primordial helium abundance ($Y = 0.246$). Moreover, they have enhanced $[\text{N}/\text{Fe}]$ by ~ 0.9 dex and are depleted by ~ 0.5 dex in both $[\text{C}/\text{Fe}]$ and $[\text{O}/\text{Fe}]$ (Mészáros et al. 2015). Photometric evidence of multiple populations along the AGB is provided by Lagioia et al. (2021), whereas the detection of multiple populations along the MS is provided by Piotto et al. (2015) and Nardiello et al. (2022), who identified a double MS in a CMD constructed with the photometry in the F275W filter of UVIS/WFC3 and the F150W NIRCam band.

Further evidence of stellar populations with different chemical compositions among giant stars comes from high-resolution spectroscopy. Star-to-star variations in carbon, oxygen, nitrogen, and sodium have been well known since the late 1970s (e.g., Sneden et al. 1991, 2000; Kraft 1994, and references therein). More recently, Mészáros et al. (2015) and Masseron et al. (2019) analyzed the elemental abundances of a large sample of giant stars of M92 from the APOGEE survey. They detected three main stellar populations with different light-element abundances, including the 1G and two groups of 2G stars. The 2G stars with extreme chemical compositions are enhanced in $[\text{Al}/\text{Fe}]$ and $[\text{Si}/\text{Fe}]$ by ~ 1.2 and ~ 0.2 dex with respect to 1G stars. These stars are also depleted in both $[\text{O}/\text{Fe}]$ and $[\text{Mg}/\text{Fe}]$ by ~ 0.5 dex when compared with the 1G. The 2G stars have intermediate chemical composition, with an aluminum content that is ~ 0.8 dex higher than that of 1G stars. They are slightly depleted in $[\text{O}/\text{Fe}]$ and $[\text{Mg}/\text{Fe}]$ and enhanced in $[\text{Si}/\text{Fe}]$ by about 0.1 dex.

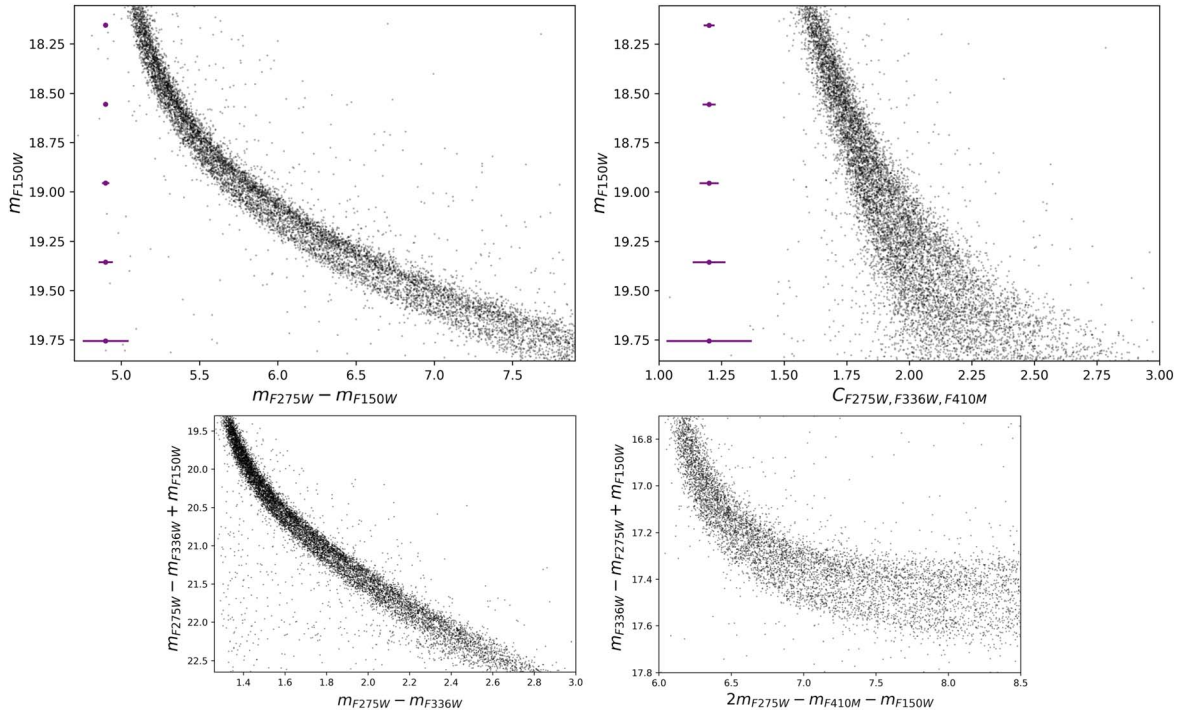


Figure 1. Top panels: m_{F150W} vs. $m_{F275W} - m_{F150W}$ (left) and m_{F150W} vs. $C_{F275W,F336W,F410M}$ (right) diagrams of MS stars. Bottom panels: $m_{F275W} - m_{F336W} + m_{F150W}$ vs. $m_{F275W} - m_{F336W}$ (left) and $m_{F336W} - m_{F275W} + m_{F150W}$ vs. $2m_{F275W} - m_{F410M} - m_{F150W}$ (right) diagrams.

In the following, we present the photometric diagrams where the multiple populations are more evident based on the diagrams constructed with the available photometric bands of WFC/ACS, UVIS/WFC3, and NIRCcam. Sections 3.1 and 3.2 are focused on bright MS stars and their kinematics, whereas Section 3.3 is dedicated to the M dwarfs.

3.1. Multiple Populations along the Main Sequence

The CMD constructed with photometry in the F275W band of UVIS/WFC3 and the F150W NIRCcam band clearly shows a split MS, and similar results are obtained by using the F814W filter of WFC3/ACS or the available NIRCcam filters (see also Nardiello et al. 2022). As shown in the top left panel of Figure 1, the two MSs are nearly mixed around the turnoff, and the $m_{F275W} - m_{F150W}$ color separation between the blue and red MS increases toward fainter magnitudes.

The $C_{F275W,F336W,F410M}$ pseudocolor is another efficient tool to identify multiple stellar populations in GCs (Milone et al. 2013). As shown in the top right panel of Figure 1, where we plot m_{F150W} against the $C_{F275W,F336W,F410M}$ pseudo-CMD, the MS is intrinsically broadened.

Evidence of multiple populations along the MS is provided by the pseudo-CMDs shown in the bottom panels of Figure 1, namely, $m_{F275W} - m_{F336W} + m_{F150W}$ versus $m_{F275W} - m_{F336W}$ and $m_{F336W} - m_{F275W} + m_{F150W}$ versus $2m_{F275W} - m_{F410M} - m_{F150W}$, which are similar to the diagrams introduced by Milone et al. (2015) for NGC 2808 but use the F410M and F150W bands instead of F438W and F814W.

To better identify multiple populations along the MS, we use the photometric diagrams plotted in the top panels of Figure 1 to construct the $\Delta_{CF275W,F336W,F410M}$ versus $\Delta_{F275W,F150W}$ ChM of MS stars, following the procedure introduced by Milone et al. (2017). Results are shown in Figure 2, where we show the ChM and corresponding Hess diagram for stars in the

MS region with $19.26 \text{ mag} < m_{F150W} < 19.56 \text{ mag}$, where multiple populations are more clearly visible.

The bulk of the stars near the origin of the ChM corresponds to the 1G, whereas 2G stars are extended toward larger values of $\Delta_{CF275W,F336W,F410M}$ and smaller values of $\Delta_{F275W,F150W}$. Clearly, 2G stars are distributed along an extended sequence and define two main stellar overdensities around $\Delta_{CF275W,F336W,F410M} \sim 0.25$ and 0.50 mag, which we call $2G_A$ and $2G_B$, respectively. The dashed lines that we determined empirically in the right panel of Figure 2 identify three stellar groups that are mostly populated by 1G, $2G_A$, and $2G_B$ stars.

The small separation between 1G and $2G_A$ stars in the ChM indicates that they share similar chemical compositions. In the context of the formation scenario proposed by Renzini et al. (2022), this evidence suggests that 1G stars did not have sufficient time to significantly pollute the interstellar medium of the cluster before the $2G_A$ population formed, indicating that $2G_A$ stars formed shortly after 1G. Conversely, the $2G_B$ population is clearly separated from the other populations, indicating a separate star formation event.

3.2. Internal Kinematics of Multiple Stellar Populations

To investigate the kinematics of the distinct stellar populations of M92, we analyzed the proper-motion dispersion of 1G, $2G_A$, and $2G_B$ stars identified in the previous section at different radial distances from the cluster center. We divided the field of view into various circular annuli by using the method of the naive estimator (Silverman 1986). Specifically, we defined a series of six points in the interval between $19''$ and $92''$ from the center of M92 separated by a distance of $d = 24''$. The bins are defined over a grid of points, which are separated by steps of $d/2$ in distance.

For each radial bin, we calculated the proper-motion velocity dispersion along the radial and tangential directions (σ_R and

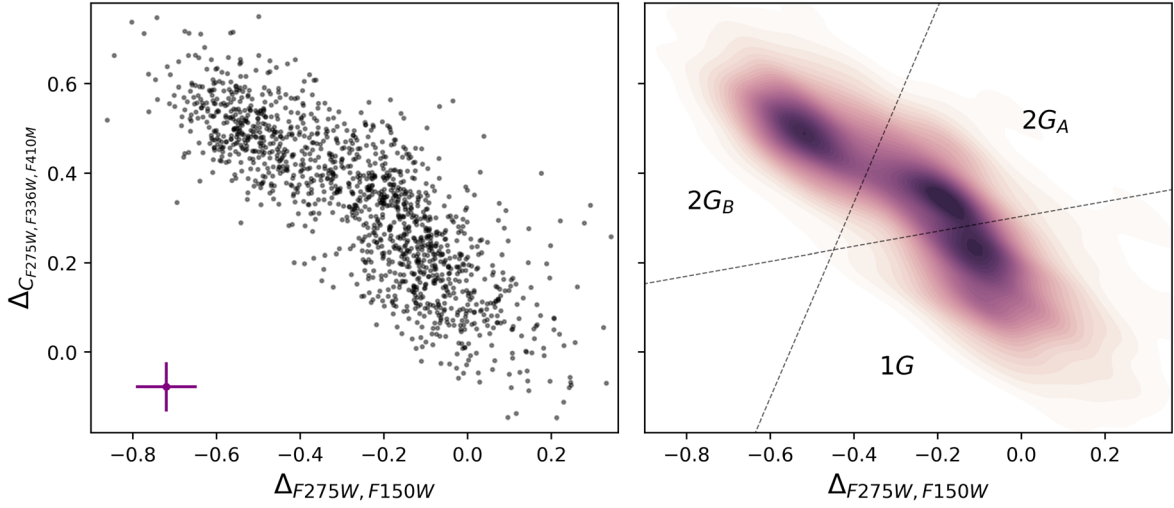


Figure 2. The $\Delta_{CF275W,F336W,F410M}$ vs. $\Delta_{F275W,F150W}$ ChM for MS stars with $19.26 \text{ mag} < m_{F150W} < 19.56 \text{ mag}$ (left panel). The corresponding Hess diagram is plotted in the right panel. The dotted lines separate the bulk of the 1G, 2G_A, and 2G_B stars.

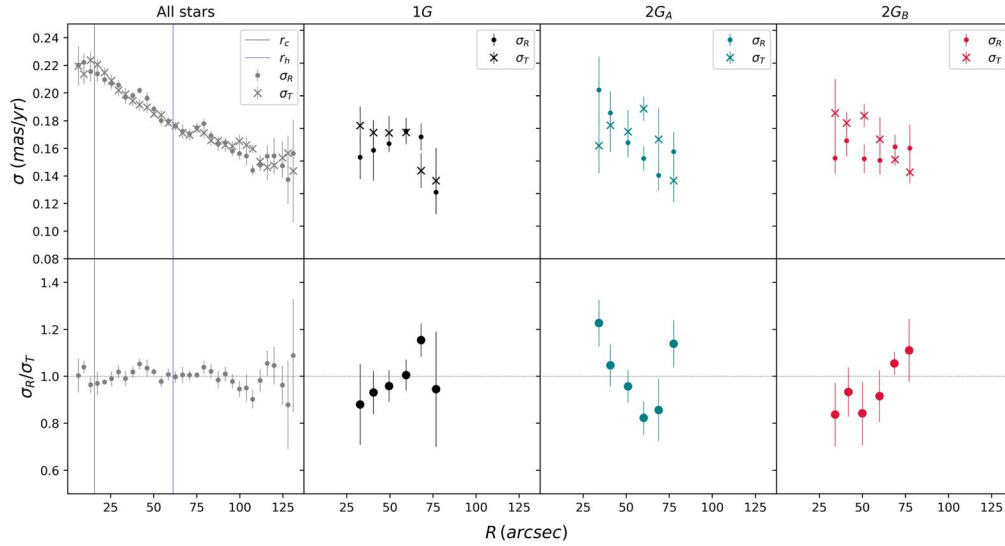


Figure 3. Velocity dispersion along the tangential (crosses) and radial (filled circles) directions as a function of the radial distance from the cluster center (top panels). Tangential to radial isotropy against the radial distance from the cluster center is shown in the bottom panels. We show results for all MS stars with $m_{F814W} < 20.0$ for 1G, 2G_A, and 2G_B stars. The two vertical lines in the left panels indicate the core radius (r_c) and half-light radius (r_h) of the cluster, respectively.

σ_T). To do that, we extended the procedure based on maximum likelihood by Mackey et al. (2013) and Marino et al. (2014) to M92. We assumed that the stellar proper motions have a normal distribution, which is described by their average value and intrinsic dispersion. The observed proper-motion distribution is also affected by measurement uncertainties. The intrinsic dispersion is inferred through the maximization of the logarithm of the joint probability function for the observed proper motions. We estimated the errors associated with the dispersion determinations by means of bootstrapping with replacements performed 1000 times. We considered the 68.27th percentile of the bootstrapped measurements as the best estimate of the proper-motion dispersion uncertainty. For completeness, we extended the procedure above to all MS stars with $m_{F814W} < 20 \text{ mag}$.

As shown in the top left panel of Figure 3, the proper-motion dispersion of all M92 stars ranges from $\sim 0.20 \text{ mas yr}^{-1}$ near the cluster center to $\sim 0.15 \text{ mas yr}^{-1}$ at a radial distance of $\sim 140''$, which corresponds to ~ 2.3 half-light radii. The 1G,

2G_A, and 2G_B stars (black, green, and red points in the top panels) share the same velocity dispersion distributions along both the tangential and radial direction. The radial interval covered by the identified 1G, 2G_A, and 2G_B stars is ~ 0.6 – 1.3 half-light radii. This radial interval is smaller than the one analyzed for all stars because it corresponds to the field where JWST and HST observations overlap. We find isotropic motions in each stellar population, as demonstrated by the fact that the ratio between σ_T and σ_R (bottom panels of Figure 3) is consistent with being ~ 1 in the analyzed radial interval.

In the past decade, work based on high-precision proper motion, mostly from HST multiepoch images and Gaia data, has investigated the internal kinematics of stellar populations in GCs (e.g., Richer et al. 2013; Libralato et al. 2023). While the 2G stars of some massive and dynamically young GCs like ω Centauri, NGC 2808, and 47 Tucanae exhibit more radially anisotropic velocity distributions than the 1G (e.g., Bellini et al. 2015, 2017; Milone et al. 2018a; Cordoni et al. 2020a), both 1G and 2G stars of other clusters exhibit nearly isotropic

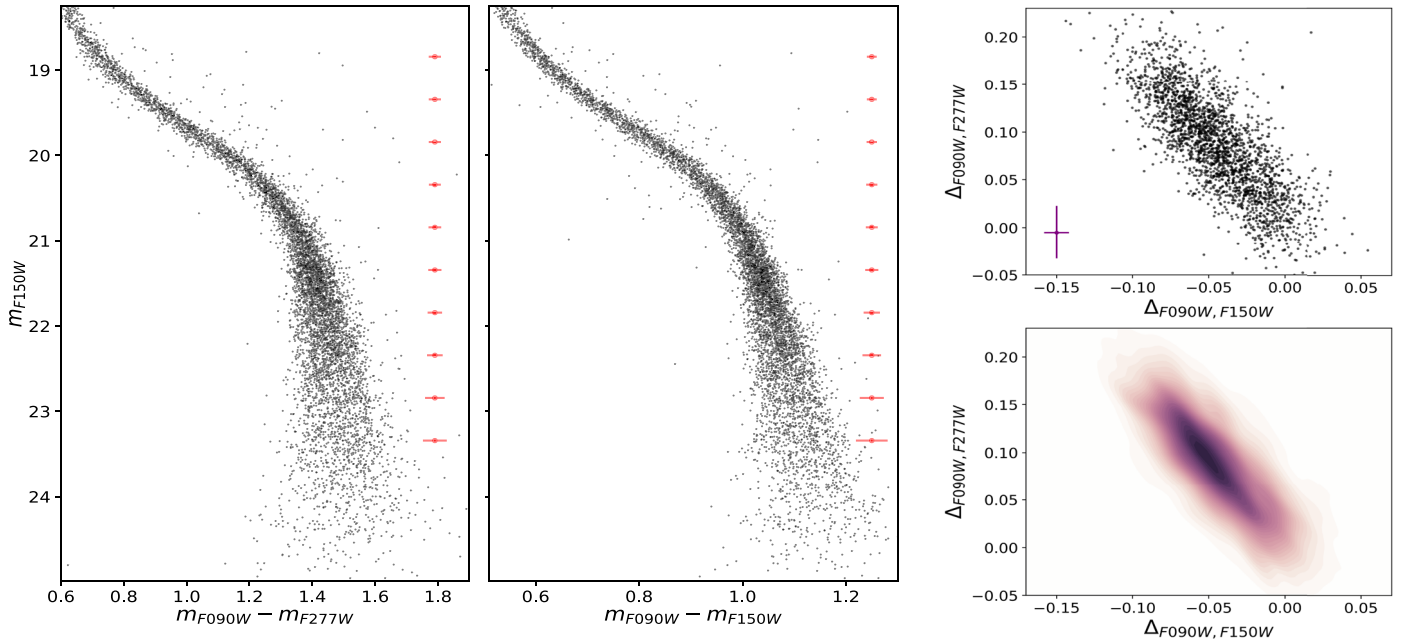


Figure 4. The m_{F150W} vs. $m_{F090W} - m_{F277W}$ (left) and m_{F150W} vs. $m_{F090W} - m_{F150W}$ (middle) CMDs of stars with a radial distance from the M92 center larger than 1/5. The right panels show the ChM for M dwarfs (top) and the corresponding Hess diagram (bottom).

velocity distributions (e.g., Libralato et al. 2019; Cordoni et al. 2020b). In a recent work, Libralato et al. (2022, 2023) derived the internal proper motions of 56 GCs and their stellar populations using multiepoch HST images. Our results on M92 stars are consistent with the results by Libralato and collaborators, who concluded that, similarly to the most dynamically evolved GCs, M92 exhibits nearly isotropic motions for radii smaller than ~ 2.5 times the half-light radius.

3.3. Multiple Populations along M Dwarfs

The CMDs constructed with the F090W, F150W, and F277W filters of NIRCcam reveal a broad MS below the knee. As illustrated in Figure 4, the color spread of M dwarfs is significantly wider than what is expected from the photometric errors alone, thus indicating the presence of multiple stellar populations among low-mass stars.

We used the m_{F150W} versus $m_{F090W} - m_{F277W}$ and m_{F150W} versus $m_{F090W} - m_{F150W}$ CMDs to construct the $\Delta_{F090W,F277W}$ versus $\Delta_{F090W,F150W}$ ChM plotted in the top right panel of Figure 4. We only considered M dwarfs with $19.26 \text{ mag} < m_{F150W} < 19.56 \text{ mag}$ (top), which is the MS region where the color broadening is more evident. As suggested by the Hess diagram (bottom right panel of Figure 4), the M dwarfs exhibit a continuous distribution in the ChM without any clear separation between 1G and 2G stars.

4. Comparison with Synthetic Model Atmospheres

To investigate the behavior of multiple stellar populations in photometric diagrams constructed with the HST filters, we derived the colors and magnitudes of the isochrones that account for the chemical compositions of 1G and 2G stars. Similar to what we did in previous papers (e.g., Milone et al. 2018b, 2023b), we selected 15 points along the isochrone that

provides the best fit with the m_{F606W} versus $m_{F606W} - m_{F814W}$ CMD of M92 and extracted the effective temperature, T_{eff} , and gravity, g , of each point. We used the isochrones from the Dartmouth database (Dotter et al. 2008) with iron abundance $[\text{Fe}/\text{H}] = -2.4$ and $[\alpha/\text{Fe}] = 0.4$ dex and adopted an age of 13.0 Gyr, distance modulus of $(m - M)_0 = 14.75$ mag, and reddening of $E(B - V) = 0.03$ mag, which are similar to the values derived by Dotter et al. (2010). We calculated models with primordial helium content, $Y = 0.246$, and enhanced helium abundances, $Y = 0.33$.

For each pair of stellar parameters, we computed a stellar atmosphere structure with ATLAS 12, which is the model atmosphere code developed by Robert Kurucz (e.g., Kurucz 1970, 1993) and ported to Linux by Sbordone et al. (2004). We computed a reference synthetic spectrum with a similar chemical composition as a 1G star (i.e., solar-scaled abundances of C and N and $[\text{O}/\text{Fe}] = 0.40$) and a comparison spectrum with $[\text{C}/\text{Fe}] = -0.5$, $[\text{O}/\text{Fe}] = -0.1$, and $[\text{N}/\text{Fe}] = 1.2$ dex, which is representative of a 2G star.

The synthetic spectra are constructed with the computer program SYNTHE (Kurucz & Avrett 1981; Castelli 2005; Sbordone et al. 2007) over the wavelength interval covered by the UVIS/WFC3, WFC/ACS, and NIRCcam filters between 2000 and 52000 Å. As an example, the black lines of Figure 5 represent the logarithm of the flux ratio between He-rich stars with 2G-like C, N, and O abundances and 1G stars at the same F115W magnitude. To display the effect of changing helium or C, N, and O alone, we show the flux ratio obtained from a He-rich star with the same C, N, and O abundances as the 1G (blue line) and the flux ratio derived from a star with 2G-like abundances of C, N, and O but primordial helium content ($Y = 0.246$; pink line). Panel (a) correspond to RGB stars with $M_{F115W} = -3.80$ mag, whereas panels (b) and (c) refer to MS stars with $M_{F115W} = 5.14$ and 8.29 mag, respectively. Clearly,

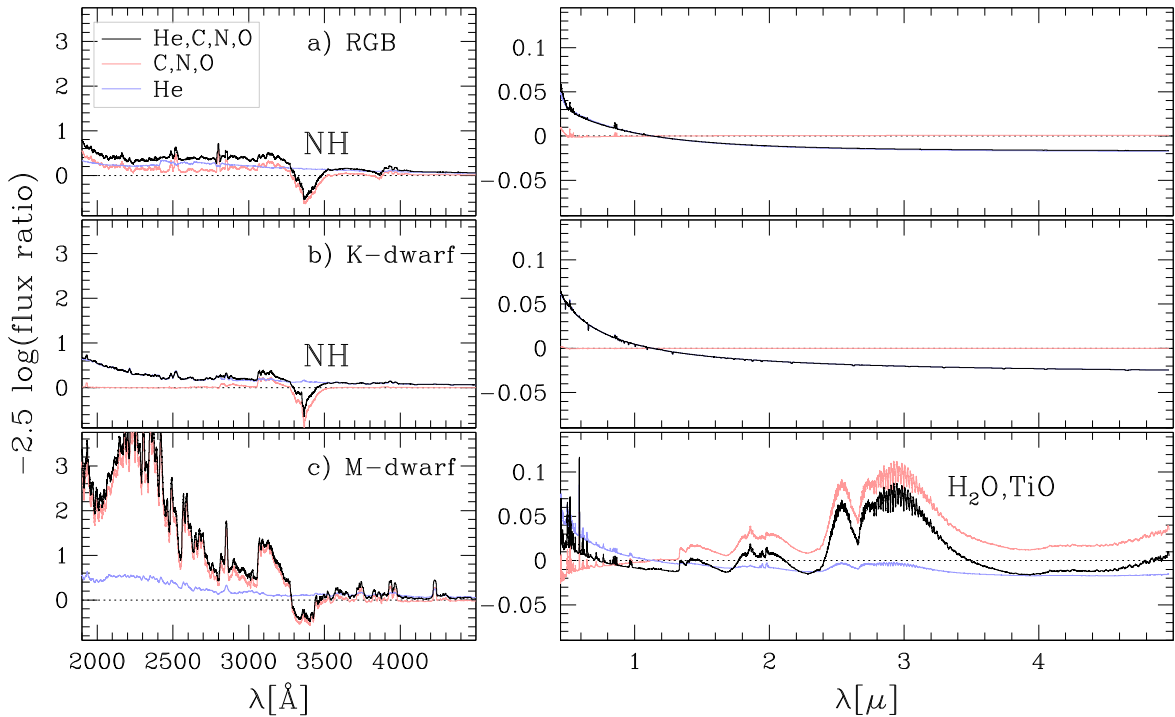


Figure 5. Flux ratio between the simulated spectra of stars with 2G-like chemical composition and the spectra of a 1G star (black lines). The pink lines correspond to spectra with the same helium content as 1G stars but different C, N, and O abundances. The blue lines are obtained from helium-enhanced stars with the same C, N, and O content as the 1G. Panels (a), (b), and (c) refer to RGB, upper MS, and M dwarf stars, respectively. We indicate the NH molecule, which is mainly responsible for the F336W magnitude difference of 2G and 1G RGB and MS stars, and the H₂O and TiO molecules that contribute to the F277W flux difference of multiple populations among M dwarfs.

in the wavelength interval covered by NIRCcam, the flux of the spectra of bright MS and RGB stars is nearly insensitive to the adopted C, N, and O variations, as demonstrated by the fact that the pink lines are close to zero. On the contrary, the fluxes of the M dwarf spectra are significantly affected by the light-element content. The most pronounced difference between 1G and 2G spectra occurs around 2.5–3.2 μm , where 2G stars exhibit higher fluxes than 1G stars with the same F115W magnitude. Other significant flux differences occur around $\lambda \sim 1.6$, ~ 2.0 , and $\gtrsim 4.6$ μm .

The simulated spectra are integrated over the transmission curves of the NIRCcam, WFC/ACS, and UVIS/WFC3 filters that are available for M92. We calculate the magnitude differences, δm_X , between each comparison spectrum and the reference spectrum. The results are illustrated in Figure 6 for the RGB, M-dwarf, and K-dwarf stars analyzed in Figure 5.

Helium variations are mostly responsible for magnitude differences between 2G and 1G stars in K dwarfs and RGB stars in the NIRCcam and HST filters. The δm value associated with helium variations monotonically decreases with the filter central wavelength, but the magnitude separation between 2G and 1G stars is much smaller in the NIR filters than the optical and UV bands. The abundances of nitrogen and oxygen mostly affect the UV spectral region. In particular, the OH molecular bands affect the F225W and F275W flux, while NH molecules are responsible for the F336W magnitude differences.

The most pronounced flux differences between 2G and 1G M dwarfs in the NIR involves the F250M, F277W, F300M, F322W2, and F323N bands and are associated with molecules composed of oxygen atoms (mostly H₂O and TiO). We find negligible magnitude variations in the F070W filter of NIRCcam and the F606W filter of WFC/ACS, in contrast with what is observed among M dwarfs with $[\text{Fe}/\text{H}] = -0.75$, where there

are large magnitude differences between 1G and 2G stars in these filters (Milone et al. 2023b).

The magnitudes of the 2G stars are derived by adding to the isochrones the corresponding values of δm_X . Some results are presented in Figure 7, where we show the isochrones in various photometric diagrams. Pink isochrones represent 1G stars ($Y = 0.246$, $[\text{C}/\text{Fe}] = 0.0$, $[\text{N}/\text{Fe}] = 0.0$, and $[\text{O}/\text{Fe}] = 0.4$), whereas black isochrones are helium enhanced with respect to the pink ones ($Y = 0.33$). Blue isochrones are indicative of 2G stars with extreme helium content ($Y = 0.33$). They are enhanced in nitrogen by 1.2 dex and depleted in both carbon and oxygen by 0.5 dex with respect to the 1G. Aqua isochrones are similar to the blue ones but have $Y = 0.246$.

The M_{F090W} versus $M_{\text{F090W}} - M_{\text{F277W}}$ CMD shown in the top left panel of Figure 7 is sensitive to oxygen variation in M dwarf atmospheres. Among the CMDs constructed with NIRCcam photometry alone, it provides a wide color separation between the photometric sequences of M dwarfs with different C, N, and O abundances. The reason is that the stellar flux in the F277W band is strongly absorbed by molecules that include oxygen, such as H₂O and TiO, whereas the F090W filter is poorly affected by these molecules. As a consequence, the 2G stars, which are O-rich, exhibit bluer $M_{\text{F090W}} - M_{\text{F277W}}$ colors than 1G stars with the same luminosity. For the same physical reason, the $M_{\text{F090W}} - M_{\text{F300M}}$ color would provide even wider color separation, although the F300M observations would need longer exposure times than the F277W ones to obtain the same signal-to-noise ratio. Similarly, the m_{F115W} versus $M_{\text{F115W}} - M_{\text{F322W2}}$ CMD would be less sensitive to multiple populations than the M_{F090W} versus $M_{\text{F090W}} - M_{\text{F277W}}$ CMD, but it could be preferable due to the shorter exposure times needed to obtain a given signal-to-noise ratio.

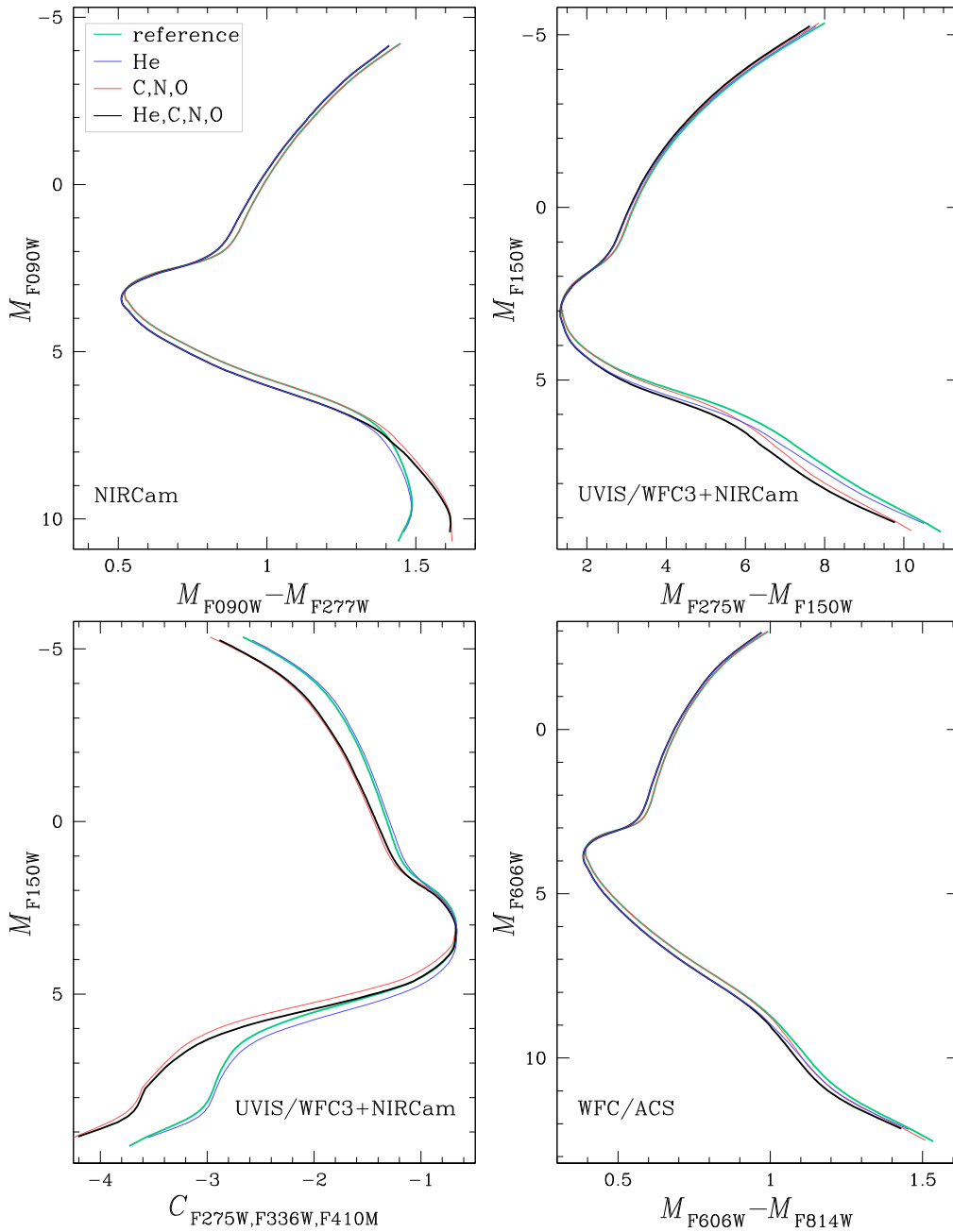


Figure 7. Isochrones with ages of 13 Gyr, $[\text{Fe}/\text{H}] = -2.3$, $[\alpha/\text{Fe}] = 0.4$, and different abundances of He, C, N, and O. The reference isochrones are shown in aqua and have the same chemical composition as 1G stars. Specifically, they have $Y = 0.246$, $[\text{C}/\text{Fe}] = 0.0$, $[\text{N}/\text{Fe}] = 0.0$, and $[\text{O}/\text{Fe}] = 0.4$. The blue isochrones have the same C, N, and O abundances as the reference isochrones but are helium enhanced ($Y = 0.33$). The pink and black isochrones have $[\text{C}/\text{Fe}] = -0.5$, $[\text{N}/\text{Fe}] = 1.2$, and $[\text{O}/\text{Fe}] = -0.1$ and helium mass fractions of $Y = 0.246$ and 0.33 , respectively.

we calculated the color difference between the fiducials of $2G_A$ and $2G_B$ stars and the 1G fiducial.

As an example, Figure 8 shows the color differences for the 19 available X filters corresponding to $m_{\text{ref}} = 19.41$. The color separation between bona fide $2G_B$ and 1G stars is maximum for $X = \text{F225W}$ and F275W , where it is larger than 0.3 mag, and steadily decreases toward the red filters. The F336W , F390M , and F390W filters, which provide narrower color differences than $m_{\text{F395N}} - m_{\text{F150W}}$, are remarkable exceptions. Noticeably, the F277W and F444W filters provide small color differences between $2G_B$ and 1G stars of about 0.01 mag. The color differences between $2G_A$ and 1G stars follow the same qualitative behavior but never exceed ~ 0.1 mag.

We used the best-fitting isochrone to extract the atmospheric parameters, T_{eff} and g , corresponding to each value of m_{ref} of 1G and 2G stars. We computed a grid of synthetic spectra for 2G stars with different abundances of He, C, N, and O using the procedure of Section 4. Each spectrum is compared with the corresponding spectrum of the 1G star, which has $Y = 0.246$, $[\text{C}/\text{Fe}] = 0.0$, $[\text{N}/\text{Fe}] = 0.0$, and $[\text{O}/\text{Fe}] = 0.4$. We assumed for the 2G spectra a set of values in $[\text{C}/\text{Fe}]$ that range from -0.5 to 0.1 dex in steps of 0.05 dex, $[\text{N}/\text{Fe}]$ between 0.0 and 1.5 in intervals of 0.1 dex, and $[\text{O}/\text{Fe}]$ that varies from -0.3 to 0.4 in steps of 0.05 dex. The adopted helium abundance varies from $Y = 0.246$ to 0.330 in steps of 0.001, and the values of T_{eff} and g are derived from the Dartmouth

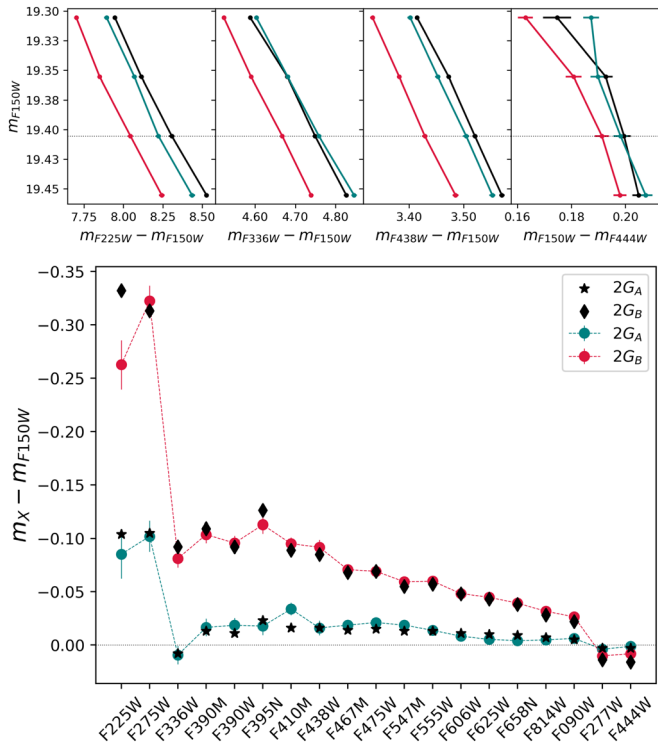


Figure 8. Top: fiducial lines of 1G (black), $2G_A$ (green), and $2G_B$ (red) stars in the m_{F150W} vs. $m_X - m_{F150W}$ (or $m_{F150W} - m_X$) planes. Here we use $X = F225W, F336W, F438W,$ and $F444W$. Bottom: $m_X - m_{F150W}$ color differences relative to the 1G fiducial for $2G_A$ (green) and $2G_B$ (red) fiducials. The latter corresponds to $m_{F150W} = 19.41$, while the filter names, X , are indicated on the x -axis. Black points represent theoretical predictions for $2G_A$ and $2G_B$ stars.

isochrone (Dotter et al. 2008). The synthetic spectra are convoluted with the transmission curves of the filters used in this paper to derive the corresponding magnitudes. The simulated color differences between the comparison and reference spectra are compared with the observed color difference between 2G and 1G stars. We assumed that the abundances of He, C, N, and O correspond to the elemental abundances of the comparison synthetic spectrum that best reproduces the observed color differences. Specifically, helium abundances are constrained from the colors constructed with optical and NIR filters, which are mostly sensitive to the effective-temperature difference associated with helium variations. Nitrogen is mainly constrained by the F336W magnitude, which encompasses the NH molecular bands, while carbon is derived from the magnitudes in the blue filters, which enclose CH and CN molecules. The F225W and F275W magnitudes are sensitive to oxygen variations through the OH molecules.

We find that $2G_A$ stars are enhanced in helium mass fraction by $\Delta Y = 0.010 \pm 0.003$ with respect to the 1G. Moreover, $2G_A$ stars have higher abundances of nitrogen ($\Delta[N/Fe] = 0.4 \pm 0.1$) and a lower content of carbon and oxygen than 1G stars ($\Delta[C/Fe] = -0.15 \pm 0.05$, $\Delta[O/Fe] = -0.25 \pm 0.05$). The $2G_B$ stars have a more extreme chemical composition than the $2G_A$ stars. They are enhanced in helium by $\Delta Y = 0.041 \pm 0.004$ and nitrogen by ($\Delta[N/Fe] = 0.8 \pm 0.1$) with respect to the 1G. When compared with the 1G, $2G_B$ stars are also depleted in carbon and oxygen by $\Delta[C/Fe] = -0.45 \pm 0.10$ and $\Delta[O/Fe] = -0.50 \pm 0.10$. Here the uncertainties are estimated

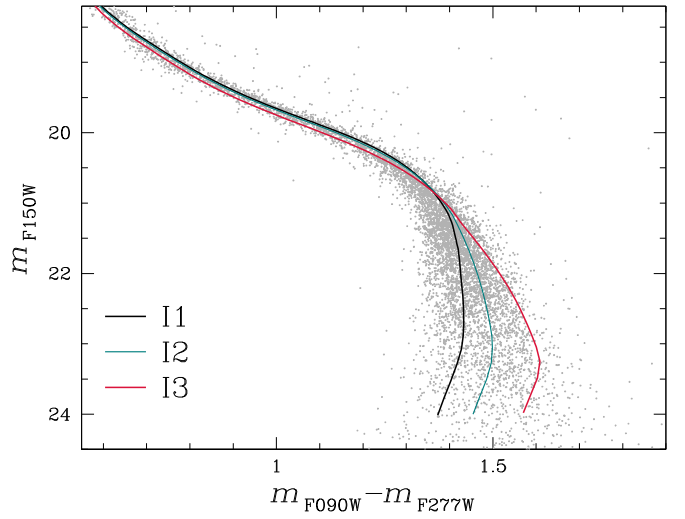


Figure 9. Best-fitting I1, I2, and I3 isochrones superimposed on the observed m_{F150W} vs. $m_{F090W} - m_{F277W}$ CMD. These three isochrones have the same age (13 Gyr) and metallicity ($[Fe/H] = -2.3$) but different contents of He, C, N, and O. Specifically, the chemical composition of the I1 isochrone is indicative of 1G stars, whereas the I2 and I3 isochrones resemble $2G_A$ and $2G_B$ stars, respectively. The faintest points in the isochrones correspond to a mass of $0.1 M_{\odot}$.

as the root mean scatter of the three elemental abundance determinations corresponding to the three reference magnitudes.

4.2. Oxygen Variations among the Low-mass Stars of M92

To constrain the chemical composition of multiple populations among the M dwarfs, we compared the m_{F150W} versus $m_{F090W} - m_{F277W}$ CMD and 13 Gyr old isochrones with the same metallicity ($[Fe/H] = -2.3$) and different light-element abundances. Indeed, as discussed in Section 4.1, for a fixed luminosity, the $m_{F090W} - m_{F277W}$ color is very sensitive to the oxygen abundance, with O-rich stars showing bluer colors. The results are illustrated in Figure 9, where the black isochrone (I1) represents 1G stars, whereas the green and red isochrones (I2 and I3) have a similar content of He, C, N, and O, as inferred for $2G_A$ and $2G_B$ RGB stars, respectively.

Although the isochrones do not provide a perfect fit of the MS segment below the knee, the $m_{F090W} - m_{F277W}$ color separation between the I1 and I2 isochrones is similar to the observed MS width, which is consistent with star-to-star oxygen variations of $[O/Fe] \sim 0.5$ dex. This fact is consistent with a scenario where stars from the same stellar population (1G or 2G) have the same oxygen abundances along the entire CMD. Indeed, the oxygen variations in M dwarfs and bright MS stars derived in this paper are comparable with those inferred for RGB stars by Sneden et al. (2000) and Mészáros et al. (2015), who obtained a similar oxygen variation of ~ 0.5 dex by means of high-resolution spectroscopy.

5. Summary and Discussion

This paper investigates multiple populations in metal-poor GCs by combining HST and JWST photometry of M92, a metal-poor GC with $[Fe/H] = -2.3$, with isochrones and synthetic spectra.

The photometric study of M92 is based on images collected through 16 filters of the UVIS/WFC3, IR/WFC3, and WFC/ACS on board HST and four NIRCcam/JWST filters. The resulting multiband photometry covers a wide wavelength

interval that ranges from the ultraviolet ($\lambda \sim 2000 \text{ \AA}$) to the infrared ($\lambda \sim 44000 \text{ \AA}$). The main results can be summarized as follows.

1. Various photometric diagrams, including the m_{F150W} versus $m_{F275W} - m_{F150W}$ CMD and the m_{F150W} versus $C_{F275W,F336W,F410M}$ pseudo-CMD, show that the color distribution of K dwarfs along the MS is either intrinsically broad or bimodal, thus revealing multiple populations. We combined these two diagrams to introduce the $\Delta_{CF275W,F336W,F410M}$ versus $\Delta_{F275W,F150W}$ ChM, which unveils three main populations of K-dwarf stars: the 1G and two groups of 2G stars, namely, $2G_A$ and $2G_B$. The $m_{F275W} - m_{F150W}$ color separation is mostly associated with differences in helium and oxygen between the stellar populations, whereas oxygen and nitrogen are mainly responsible for the $C_{F275W,F336W,F410M}$ MS width. Indeed, the F275W band encloses OH molecular bands, whereas the F336W filter includes NH bands.
2. We analyzed the internal kinematics of the stellar populations in M92 by using stellar proper motions. The three stellar populations share similar radial distributions of the proper-motion dispersion that range from about 0.2 mas yr^{-1} near the cluster center to 0.15 mas yr^{-1} around a distance of ~ 2.2 half-light radii. The 1G, $2G_A$, and $2G_B$ stars exhibit isotropic motions in the studied radial interval within ~ 1.5 half-light radii. These results corroborate similar conclusions by Libralato et al. (2022, 2023) based on RGB stars.
3. We analyzed multiple populations in 19 m_{F150W} versus $m_X - m_{F150W}$ (or $m_{F150W} - m_X$) CMDs, where X indicates the available photometric bands. We compared the observed colors of 1G and 2G stars and the colors derived from grids of synthetic spectra to infer the average helium abundance of each population. We find that $2G_A$ and $2G_B$ stars have higher helium mass fractions by $\Delta Y = 0.010 \pm 0.003$ and 0.041 ± 0.004 , respectively, than the 1G, for which we assumed a primordial helium abundance of $Y = 0.246$. The helium difference between $2G_B$ and 1G MS stars is consistent with the maximum helium variation inferred for RGB stars ($\Delta Y = 0.039 \pm 0.006$; Milone et al. 2018b).
4. The m_{F150W} versus $m_{F090W} - m_{F277W}$ and m_{F150W} versus $m_{F090W} - m_{F150W}$ CMDs reveal that MS stars fainter than the MS knee exhibit an intrinsic color spread, which is present among stars with masses of about $\sim 0.1\text{--}0.4 M_\odot$. The color broadening is due to stellar populations with different oxygen abundances. These low-mass stars exhibit a continuous color distribution and do not show evidence for distinct groups of 1G and 2G stars. The MS width is consistent with star-to-star oxygen variations of $[O/Fe] \sim 0.5$ dex. This value is similar to the oxygen difference between $2G_B$ and 1G stars we inferred for K dwarfs. Moreover, it matches the oxygen interval detected among RGB stars from high-resolution spectroscopy (e.g., Sneden et al. 2000; Mészáros et al. 2015). The evidence of multiple populations presenting similar chemical composition among stars with different masses corroborates the results obtained for 47 Tucanae (Milone et al. 2023b), challenging formation scenarios that predict that GC stars are coeval and the chemical

composition of 2G stars is a product of accretion of polluted material onto pre-MS stars (Gieles et al. 2018).

To investigate the behavior of multiple populations of metal-poor GCs in CMDs constructed with NIRCcam filters and the WFC/ACS and UVIS/WFC3 on board HST, we derived isochrones with $[Fe/H] = -2.3$ and different abundances of He, C, N, and O. Similar to what we found for metal-intermediate GCs with $[Fe/H] = -0.75$ and -1.5 , the photometric diagrams made with NIRCcam filters alone do not allow us to disentangle stellar populations with different abundances of C, N, and O along the RGB, the subgiant branch, and the MS regions above the MS knee. The 2G MS and RGB stars with large helium abundances ($Y = 0.33$) exhibit bluer colors than 1G stars with the same luminosity, but their color difference obtained from photometry in the NIRCcam bands alone is typically smaller than ~ 0.05 mag.











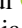
On the contrary, NIRCcam photometry can be a powerful tool to identify 1G and 2G stars below the MS knee, where various colors, including F090W – F300M, F090W – F277W, and F090W – F322W2 allow one to identify 1G and 2G M dwarfs with different oxygen abundances. Optical filters, such as the F070W band of NIRCcam or the F606W filters of WFC/ACS and UVIS/WFC3 on board HST, have poor sensitivity to C, N, and O content variations among M dwarfs. This is in contrast to the results of isochrones with $[Fe/H] = -0.75$ and observations of 47 Tucanae, which show large F070W and F606W magnitude differences between 1G and 2G stars with different oxygen abundances (Milone et al. 2023b).

Acknowledgments

This work has received funding from the European Union’s Horizon 2020 research and innovation program under Marie Skłodowska-Curie grant agreement No. 101034319 and from the European Union—NextGenerationEU, beneficiary: Ziliotto. A.P.M. and E.D. have been supported by MIUR under PRIN program 2017Z2HSMF (PI: Bedin).

All of the data presented in this paper were obtained from the Mikulski Archive for Space Telescopes (MAST) at the Space Telescope Science Institute. The specific observations analyzed can be accessed via doi:10.17909/7se9-0540.

ORCID iDs

Tuila Ziliotto  <https://orcid.org/0000-0001-8538-2068>
 Antonino Milone  <https://orcid.org/0000-0001-7506-930X>
 Anna F. Marino  <https://orcid.org/0000-0002-1276-5487>
 Aaron L. Dotter  <https://orcid.org/0000-0002-4442-5700>
 Alvio Renzini  <https://orcid.org/0000-0002-7093-7355>
 Amanda Karakas  <https://orcid.org/0000-0002-3625-6951>
 Giacomo Cordoni  <https://orcid.org/0000-0002-7690-7683>
 Emanuele Dondoglio  <https://orcid.org/0000-0001-8415-8531>
 Maria V. Legnardi  <https://orcid.org/0000-0003-3153-1499>
 Edoardo P. Lagioia  <https://orcid.org/0000-0003-1713-0082>
 Anjana Mohandasan  <https://orcid.org/0000-0001-5182-0330>

References

- Anderson, J., Bedin, L. R., Piotto, G., Yadav, R. S., & Bellini, A. 2006, *A&A*, 454, 1029
 Anderson, J., & King, I. R. 2006, PSFs, Photometry, and Astronomy for the ACS/WFC, Instrument Sci. Rep. ACS 2006-01, 34

- Bastian, N., Lamers, H. J. G. L. M., de Mink, S. E., et al. 2013, *MNRAS*, **436**, 2398
- Bastian, N., & Lardo, C. 2018, *ARA&A*, **56**, 83
- Bellini, A., Anderson, J., & Bedin, L. R. 2011, *PASP*, **123**, 622
- Bellini, A., Anderson, J., Bedin, L. R., et al. 2017, *ApJ*, **842**, 6
- Bellini, A., & Bedin, L. R. 2009, *PASP*, **121**, 1419
- Bellini, A., Vesperini, E., Piotto, G., et al. 2015, *ApJL*, **810**, L13
- Calura, F., D’Ercole, A., Vesperini, E., Vanzella, E., & Sollima, A. 2019, *MNRAS*, **489**, 3269
- Castelli, F. 2005, *MSAIS*, **8**, 25
- Cordoni, G., Milone, A. P., Marino, A. F., et al. 2020a, *ApJ*, **898**, 147
- Cordoni, G., Milone, A. P., Mastrobuono-Battisti, A., et al. 2020b, *ApJ*, **889**, 18
- Cottrell, P. L., & Da Costa, G. S. 1981, *ApJL*, **245**, L79
- Dantona, F., Gratton, R., & Chieffi, A. 1983, *MmSAI*, **54**, 173
- D’Antona, F., Vesperini, E., D’Ercole, A., et al. 2016, *MNRAS*, **458**, 2122
- Decressin, T., Meynet, G., Charbonnel, C., Prantzos, N., & Ekström, S. 2007, *A&A*, **464**, 1029
- Denissenkov, P. A., & Hartwick, F. D. A. 2014, *MNRAS*, **437**, L21
- Dondoglio, E., Milone, A. P., Renzini, A., et al. 2022, *ApJ*, **927**, 207
- Dotter, A., Chaboyer, B., Jevremović, D., et al. 2008, *ApJS*, **178**, 89
- Dotter, A., Sarajedini, A., Anderson, J., et al. 2010, *ApJ*, **708**, 698
- Gaia Collaboration, Brown, A. G. A., Vallenari, A., et al. 2021, *A&A*, **649**, A1
- Gieles, M., Charbonnel, C., Krause, M. G. H., et al. 2018, *MNRAS*, **478**, 2461
- Gilliland, R. L. 2004, ACS CCD Gains, Full Well Depths, and Linearity up to and Beyond Saturation, Instrument Science Report ACS 2004-01, 34
- Gratton, R., Bragaglia, A., Carretta, E., et al. 2019, *A&ARv*, **27**, 8
- Harris, W. E. 1996, *AJ*, **112**, 1487
- Jang, S., Milone, A. P., Legnardi, M. V., et al. 2022, *MNRAS*, **517**, 5687
- Kraft, R. P. 1994, *PASP*, **106**, 553
- Kurucz, R. L. 1970, SAO Special Report, 309
- Kurucz, R. L. 1993, SYNTHE Spectrum Synthesis Programs and Line Data (Kurucz CD-ROM)
- Kurucz, R. L., & Avrett, E. H. 1981, SAO Special Report, 391
- Lagioia, E. P., Milone, A. P., Marino, A. F., & Dotter, A. 2019, *ApJ*, **871**, 140
- Lagioia, E. P., Milone, A. P., Marino, A. F., et al. 2021, *ApJ*, **910**, 6
- Lee, J.-W. 2022, *ApJS*, **263**, 20
- Legnardi, M. V., Milone, A. P., Armillotta, L., et al. 2022, *MNRAS*, **513**, 735
- Libralato, M., Bellini, A., Piotto, G., et al. 2019, *ApJ*, **873**, 109
- Libralato, M., Bellini, A., Vesperini, E., et al. 2022, *ApJ*, **934**, 150
- Libralato, M., Vesperini, E., Bellini, A., et al. 2023, *ApJ*, **944**, 58
- Mackey, A. D., Da Costa, G. S., Ferguson, A. M. N., & Yong, D. 2013, *ApJ*, **762**, 65
- Marino, A. F., Milone, A. P., Renzini, A., et al. 2019, *MNRAS*, **487**, 3815
- Marino, A. F., Milone, A. P., Yong, D., et al. 2014, *MNRAS*, **442**, 3044
- Marino, A. F., Villanova, S., Piotto, G., et al. 2008, *A&A*, **490**, 625
- Masseron, T., García-Hernández, D. A., Mészáros, S., et al. 2019, *A&A*, **622**, A191
- Mészáros, S., Martell, S. L., Shetrone, M., et al. 2015, *AJ*, **149**, 153
- Milone, A. P., Cordoni, G., Marino, A. F., et al. 2023a, *A&A*, **672**, A161
- Milone, A. P., & Marino, A. F. 2022, *Univ*, **8**, 359
- Milone, A. P., Marino, A. F., Bedin, L. R., et al. 2019, *MNRAS*, **484**, 4046
- Milone, A. P., Marino, A. F., Cassisi, S., et al. 2012a, *ApJL*, **754**, L34
- Milone, A. P., Marino, A. F., Dotter, A., et al. 2023b, *MNRAS*, **522**, 2429
- Milone, A. P., Marino, A. F., Mastrobuono-Battisti, A., & Lagioia, E. P. 2018a, *MNRAS*, **479**, 5005
- Milone, A. P., Marino, A. F., Piotto, G., et al. 2013, *ApJ*, **767**, 120
- Milone, A. P., Marino, A. F., Piotto, G., et al. 2015, *ApJ*, **808**, 51
- Milone, A. P., Marino, A. F., Renzini, A., et al. 2018b, *MNRAS*, **481**, 5098
- Milone, A. P., Marino, A. F., Renzini, A., et al. 2020, *MNRAS*, **497**, 3846
- Milone, A. P., Piotto, G., Bedin, L. R., et al. 2012b, *ApJ*, **744**, 58
- Milone, A. P., Piotto, G., Renzini, A., et al. 2017, *MNRAS*, **464**, 3636
- Monelli, M., Milone, A. P., Stetson, P. B., et al. 2013, *MNRAS*, **431**, 2126
- Nardiello, D., Bedin, L. R., Burgasser, A., et al. 2022, *MNRAS*, **517**, 484
- Piotto, G., Milone, A. P., Anderson, J., et al. 2012, *ApJ*, **760**, 39
- Piotto, G., Milone, A. P., Bedin, L. R., et al. 2015, *AJ*, **149**, 91
- Renzini, A., Marino, A. F., & Milone, A. P. 2022, *MNRAS*, **513**, 2111
- Richer, H. B., Heyl, J., Anderson, J., et al. 2013, *ApJL*, **771**, L15
- Salaris, M., Cassisi, S., Mucciarelli, A., & Nardiello, D. 2019, *A&A*, **629**, A40
- Sbordone, L., Bonifacio, P., & Castelli, F. 2007, in IAU Symp. 239, Convection in Astrophysics, ed. F. Kupka, I. Roxburgh, & K. L. Chan (Cambridge: Cambridge Univ. Press), 71
- Sbordone, L., Bonifacio, P., Castelli, F., & Kurucz, R. L. 2004, *MSAIS*, **5**, 93
- Sbordone, L., Salaris, M., Weiss, A., & Cassisi, S. 2011, *A&A*, **534**, A9
- Silverman, B. W. 1986, Density Estimation for Statistics and Data Analysis (London: Chapman and Hall)
- Snedden, C., Kraft, R. P., Prosser, C. F., & Langer, G. E. 1991, *AJ*, **102**, 2001
- Snedden, C., Pilachowski, C. A., & Kraft, R. P. 2000, *AJ*, **120**, 1351
- VandenBerg, D. A. 2022, *MNRAS*, **518**, 4517
- Yong, D., Grundahl, F., Johnson, J. A., & Asplund, M. 2008, *ApJ*, **684**, 1159
- Zennaro, M., Milone, A. P., Marino, A. F., et al. 2019, *MNRAS*, **487**, 3239